Metallic Inverse Opal Frameworks as Catalyst Supports for High-Performance Water Electrooxidation

Tam D. Nguyen,[a, b] Dijon A. Hoogeveen,[a] Pavel V. Cherepanov,[a] Khang N. Dinh,[a] Daniel van Zeil,[a] Joseph F. Varga,[b] Douglas R. MacFarlane,*[a] and Alexandr N. Simonov*[a]

High intrinsic activity of oxygen evolution reaction (OER) catalysts is often limited by their low electrical conductivity. To address this, we introduce copper inverse opal (IO) frameworks offering a well-developed network of interconnected pores as highly conductive high-surface-area supports for thin catalytic coatings, for example, the extremely active but poorly conducting nickel-iron layered double hydroxides (NiFe LDH). Such composites exhibit significantly higher OER activity in 1 M KOH than NiFe LDH supported on a flat substrate or deposited as inverse opals. The NiFe LDH/Cu IO catalyst enables oxygen evolution rates of 100 mA cm^{-2} (727 ± 4 A $g_{catalyst}^{-1}$) at an overpotential of 0.305 ± 0.003 V with a Tafel slope of 0.044 ± 0.002 V dec^{-1}. This high performance is achieved with 2.2 ± 0.4 μm catalyst layers, suggesting compatibility of the inverse-opal-supported catalysts with membrane electrolyzers, in contrast to similarly performing 10^3-fold thicker electrodes based on foams and other substrates.

Introduction

The intermittency and geographic isolation of renewable energy resources motivates the development of technologies for their conversion into high-energy-density fuels to support global distribution of the sustainable energy.[1] In this context, renewable-powered electrochemical water splitting into clean hydrogen fuel and oxygen is recognized as a process of core interest by both academia[1,2] and industry.[3] Of the two half-reactions comprising the water electrolysis process, the anodic oxygen evolution reaction (OER) is more kinetically hindered, which has stimulated intense research on the development of new OER catalysts.[4]

Traditional alkaline water electrolyzers[5] and the emerging alkaline-exchange membrane (AEM) devices[6] benefit from the use of relatively low-cost electrocatalysts, the most effective of which are commonly based on nickel.[7] For the anodes, of particular note are nickel-iron layered double hydroxides (LDH) that have been demonstrated to exhibit very high intrinsic catalytic activity.[8] NiFe LDH are two-dimensional layered materials of low cost that can be prepared at scale using a range of methods,[8b,9] including by electrodeposition.[10] However, the performance of NiFe LDH and other (hydro)oxide/oxyhydroxide catalysts at high current densities, as required for practical electrolysis, is limited by their low electrical conductivity.[11] A traditional approach to resolve this is immobilization of a dispersed catalyst on a high surface area and highly conductive support, which also increases the active surface area and thereby improves the performance. In the light of instability of the otherwise advantageous carbon supports under electrooxidative conditions[12] metals and metal oxides present the most technologically viable options as supporting materials for the OER catalysts.[13] Often, these supports are based on nickel, such as Ni metal foam,[14] $NiCo_2O_4$,[15] $NiCo_2S_4$[16] or NiFe[17] nanowires (NWs), Ni_3N sheets,[18] and others. Other materials, for example 2D titanium carbide and MoS_2 have also been reported as effective supports for NiFe LDH-based catalysts.[19] Another support material of interest is copper metal due to its outstanding conductivity,[20] although compounds like Cu_2O NWs[21] and Cu_3P nanoarrays[22] were also demonstrated to be effective.

Another important characteristic of an electrocatalyst support is its texture, which defines the mass-transport of the reactant (OH^-) and product (O_2) during the OER and therefore can be tuned to enhance the performance. Recently, several research teams have reported on the OER catalysts with an inverse opal (IO) morphology, which presents high surface area provided by large (a few hundred nm) pores within a mechanically strong monolithic framework. The materials of this class reported so far include both free-standing IO catalysts (Ni IO,[23] IrO_2 IO,[24] C–Co_3O_4 IO[25] and NiFeMo IO[26]), as well as IO-supported systems (Fe:Ni/Ni_2P IO,[27] Ir/Sb:SnO_2 IO[28] and $NiCoO_2$/$NiCo_2O_4$ IO[29]). Arguably, the latter approach presents the most effective strategy to utilize the advantages of the inverse opal materials, which address key requirements for an "ideal" catalyst support: large surface area to immobilize highly dispersed active species, large channels facilitating mass transport and high electrical conductivity.

[a] Dr. T. D. Nguyen, Dr. D. A. Hoogeveen, Dr. P. V. Cherepanov, Dr. K. N. Dinh, D. van Zeil, Prof. D. R. MacFarlane, Dr. A. N. Simonov
School of Chemistry
Monash University
Clayton, VIC 3800 (Australia)
E-mail: douglas.macfarlane@monash.edu
alexandr.simonov@monash.edu
[b] Dr. T. D. Nguyen, Dr. J. F. Varga
Energys Australia Pty Ltd
2 Anzed Court, Mulgrave, VIC 3170 (Australia)

Supporting information for this article is available on the WWW under https://doi.org/10.1002/cssc.202200858

The feature shared by previous studies of the IO catalysts is the use of polystyrene (PS) sacrificial template, the cost of which can be quite high, particularly for the monodispersed hydrophilized PS beads required to produce highly ordered structures.[30] A cheaper alternative is poly(methyl methacrylate) (PMMA), which can be synthesized in a one-step procedure[31] and then removed by low-cost dichloromethane solvent.

The present work aims to combine the advantages of the Ni–Fe hydroxide catalyst, metallic copper support and inverse opal morphology produced using cheap PMMA template to achieve more than an order of magnitude improvements in the mass-normalized OER activity with micron-thick catalyst layers that are compatible with AEM electrolyzers.

Results and Discussion

The electrode synthesis procedure employed herein is summarized in Figure S1 in the Supporting Information and the Experimental Section. As a conductive reusable substrate, we employed glass sheets coated with fluorine-doped tin(IV) oxide (FTO), which is suitable for the decal transfer of IO catalyst layers onto ion-exchange membranes.[24] Scanning electron microscopic (SEM) analysis of the FTO electrodes functionalized with the template layer confirmed the uniform size distribution of the PMMA opals with a diameter of 430 ± 10 nm and their condensed and compact packing on the surface (Figures 1a and S2a). Electrodeposition of copper onto the PMMA/FTO and subsequent removal of the template produced a metallic inverse opal structure (Figure 1b) at a low mass loading of 0.045 ± 0.003 mg cm^{-2}. The void space of the Cu IO framework was 411 ± 12 nm (Figure S2b), matching the original PMMA opal size and indicating no significant shrinkage of the metal. High interconnectivity of the framework is evidenced by the holes linking all of the visible voids in Figure 1b. The size of the Cu IO voids used herein was considered sufficiently wide to allow for the deposition of a catalyst layer without blocking the interconnected pores (see below), while not excessively large to decrease the surface area per unit volume of the electrode layer. These results demonstrate that a macroporous IO structure can be obtained using a low cost PMMA opal template, rather than the more expensive hydrophilized polystyrene suspensions. Given the favorably low amounts of Cu IO deposited, measurements of the specific surface area (A [m^2 g^{-1}]) of the framework by traditional low-temperature gas adsorption and porosimetry techniques were not feasible. At the same time, high uniformity of the produced layers allows for a reasonable estimate of the geometric area of the copper inverse opal structure to be made, using the values of average pore diameter, $D = (411 \pm 12) \times 10^{-9}$ m, pore density per unit volume, $\sigma = (2.5 \pm 0.2) \times 10^{19}$ m^{-3} (both derived from the SEM analysis), density of Cu metal, $\rho = 9 \times 10^6$ g m^{-3}, and the formula $A = \frac{\sigma \pi D^2}{(1 - \sigma \frac{\pi D^3}{6}) \rho}$. The resulting value calculated for Cu IO is ca. 16 m^2 g$_{Cu}^{-1}$, which is reasonably high for such a dense material like copper. Moreover, one should note that this calculation does not account for any additional meso-/microporosity of the surface, which is typically making a major contribution to the A values determined by gas adsorption techniques.

Functionalization of the Cu IO framework with NiFe LDH nanosheets (Figure 1c) by reductive electrodeposition[10b,c] decreased the void diameter to 240 ± 20 nm, which corresponds to the thickness of the catalyst layer of 85 ± 14 nm (Figure S2c).

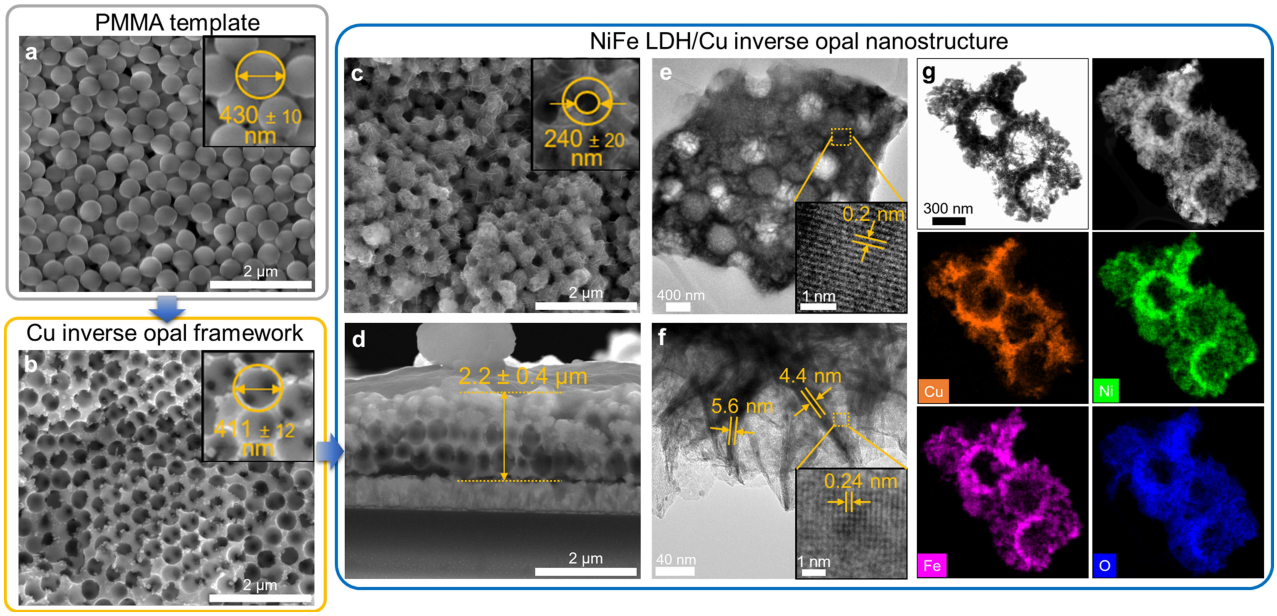

Figure 1. Microscopic characterization of the a) PMMA template layer, b) Cu inverse opal framework, and c–f) NiFe LDH / Cu IO composite deposited onto a FTO electrode: a–c) top-view and d) cross-sectional SEM images, e–f) lower (main panels) and higher (insets) magnification TEM images focusing on the e) overall NiFe LDH / Cu IO composite and f) NiFe LDH nanosheets, and g) STEM-EDS mapping.

The overall CuIO support + NiFeLDH catalyst loading for the resulting electrodes was only 0.14 ± 0.04 mg cm^{-2}, that is, the mass of the catalytic component was approximately twice higher than that of the copper framework. Cross-sectional SEM imaging demonstrated homogeneous deposition of NiFeLDH throughout the whole CuIO layer with the thickness of only 2.2 ± 0.4 μm (Figure 1d). Energy dispersive X-ray spectroscopy (EDS) confirmed the presence of copper, nickel, and iron, with uniform distribution of the catalyst over the support (Figure S3). Transmission electron microscopic (TEM) analysis corroborated the SEM observations of the homogeneous functionalization of the copper surface with the hydroxide nanosheets and highlighted the high degree of their interconnection (Figure 1e,f). When focusing on the Cu framework areas in the TEM images, distinctive lattice fringes with an interplanar spacing of ca. 0.2 nm corresponding to the (111) plane of metallic copper[32] were observed (inset to Figure 1e). The NiFeLDH sheets were predominantly thinner than 10 nm and did not exhibit distinctive lattice fringes, except for rare areas where an interlayer spacing of about 0.24 nm was measured (Figure 1f). Such *d*-spacing can be attributed to NiO,[33] which might be present as a minor component. The scanning TEM-EDS (STEM-EDS) mapping corroborates the homogenous coating of the CuIO framework with NiFeLDH (Figure 1g).

Control NiFeLDH IO samples were obtained by directly depositing the electrocatalyst onto the PMMA opal template, that is, omitting the Cu electrodeposition step. Electrodes prepared in this manner had a catalyst loading of 0.20 ± 0.02 mg cm^{-2} and also exhibited an inverse opal structure with an average pore size of 430 ± 20 nm, similar to the CuIO (Figures S2d and S4a). However, such approach does not produce abundant high surface area nanosheets as in the case of NiFeLDH/CuIO since the PMMA template promotes the formation of a smooth inner-void surface. Another type of control samples was synthesized by using an unmodified, PMMA-free FTO substrate to produce NiFeLDH/Cu thin film (TF) materials, where the catalyst nanosheets were formed as uniform and compact layers on the copper-modified FTO (Figure S4c,d).

X-ray diffraction (XRD) patterns of CuIO and NiFeLDH/CuIO exhibited peaks corresponding to copper metal (COD 5000216), on top of the diffraction signals associated with the FTO substrate (Figure S5a). Introduction of NiFeLDH did not produce detectable changes to the structure of CuIO but only induced the emergence of a weak peak at 52.6°, which can be attributed to metallic Ni (COD 9008476) and/or Fe (COD 9000659). The same XRD signal was found for the NiFeLDH IO control samples (Figure S6), and is attributed to partial reduction of the precursors during the NiFeLDH electrodeposition.[34] No other diffraction peaks corresponding to the transition metal phases were observed in the XRD patterns of NiFeLDH/CuIO and NiFeLDH IO, notwithstanding the mass of nickel-iron hydroxide material deposited was notably higher than that of the copper, which produced well-defined diffraction signals (Figure S5a). These results further confirm the predominantly amorphous nature of the produced layered double hydroxide catalyst layers, consistent with the microstructural analysis by TEM (Figure 1f).

X-ray photoelectron spectroscopic (XPS) analysis of NiFeLDH/CuIO confirmed the presence of Ni and Fe, but also enabled the detection of Cu (Figure S5b–d; extended XPS data are provided in Figure S7), suggesting that parts of CuIO were coated with very thin NiFeLDH layers. However, these regions present a very small fraction of the support surface as they could not be observed by SEM. The major components of the Cu 2p peaks were consistent with the metallic copper state, while weak shoulders at higher binding energies and a shake-up peak attest to the expected presence of a minor oxidized component.[35] Ni and Fe were quantified by XPS to be present at essentially equal amounts, which matches their ratio in the precursor solution (Figure S7d). Ni 2p and Fe 2p spectra were consistent with those of the corresponding hydroxides/oxides,[36] but also exhibited low-intensity signals at 852.5 and 706.5 eV associated with metallic Ni and Fe, respectively. The presence of the latter is consistent with the XRD observations as explained above.

Voltammetric characterization of NiFeLDH/CuIO in stirred O_2-saturated 1 M KOH demonstrated their notably higher OER catalytic activity as compared to CuIO, NiFeLDH/CuTF and NiFeLDH IO, both with (Figure 2a) and without (Figure S8a) correction for ohmic losses applied (using uncompensated resistance, R_u, measured by electrochemical impedance spectroscopy, EIS). The true[37] initial electrocatalytic performance derived from the short-term chronopotentiometric measurements (Figures 2b and S8b) and presented as polarization plots (Figures 2c and S8c) more reliably confirms the significant promoting effect of the CuIO framework. The OER charge transfer resistance (R_{ct}) values derived from fitting the experimental EIS data collected at the OER overpotential (η) of 0.25 V with simulations based on a $R_u[R_{ct}||\text{CPE}]$ circuit (CPE is a constant phase element used to model the double-layer capacitance) followed the expected trend with the lowest R_{ct} for NiFeLDH/CuIO (Table S1). The performance of the catalysts was highly reproducible as confirmed through tests of 3 independent samples of each type (Figure 2b,c). We also explored the effect of the nickel:iron ratio on the activity of NiFeLDH/CuIO and found that the 1:1 composition provides the best results under conditions employed (Figure S9).

Introduction of the Cu support expectedly decreased R_u for NiFeLDH/CuTF and NiFeLDH/CuIO as compared to NiFeLDH IO directly deposited onto FTO (Figure 2d, Table S1). However, even upon applying the corresponding iR_u-corrections, the electrodes with no Cu demonstrated a resistance-controlled performance in voltammetry (Figure 2a) and steady-state current density (j) vs. potential plots (Figure 2c). Specifically, the (E-iR_u) vs. log j dataset for NiFeLDH/CuIO maintained linearity up to high current densities of 100 mA cm^{-2} with a low slope of 0.044 ± 0.002 V dec^{-1}. This contrasts the higher slopes for NiFeLDH IO (0.075 ± 0.005 V dec^{-1}) and NiFeLDH/CuTF (0.072 ± 0.005 V dec^{-1}) and the loss of linearity at $j > 10$ mA cm^{-2}, which is indicative of hampered electron transfer through the catalyst layer at high current densities.[11] This problem does apply to the NiFeLDH/CuIO electrodes due to the unique structure

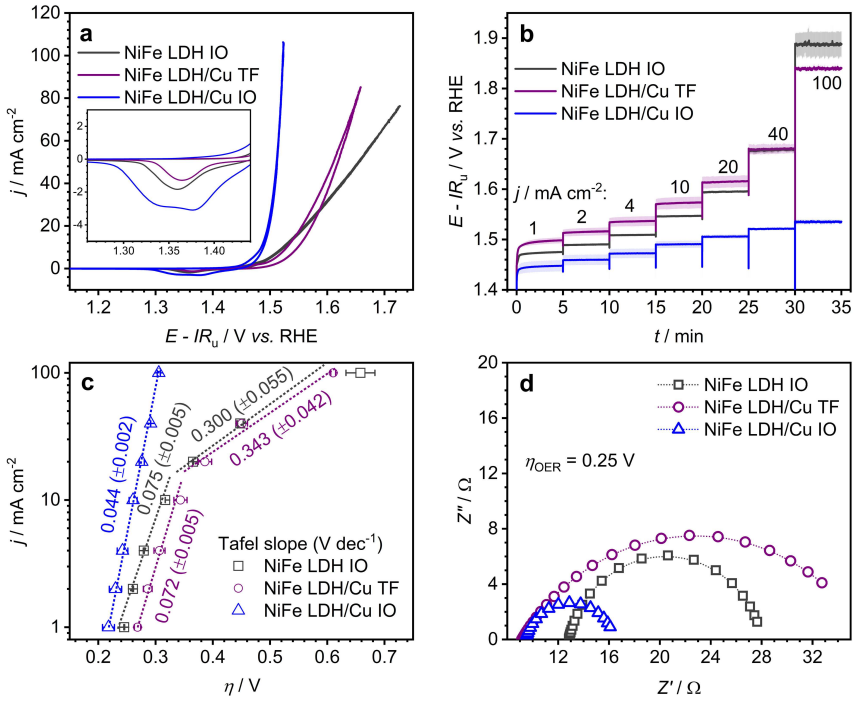

Figure 2. Electrochemical characterization of FTO functionalized with NiFe LDH IO (grey), NiFe LDH / Cu TF (purple) and NiFe LDH / Cu IO (blue) in stirred O_2-saturated 1 M KOH. a) Cyclic voltammograms ($v = 0.010$ V s^{-1}; 3rd scans); inset shows the expanded plot of the NiFe LDH reduction processes. b) Quasi-steady-state chronopotentiograms at current densities specified in the plot, and c) corresponding polarization plots with symbols and lines showing experimental data and linear fits, respectively, while values are the corresponding Tafel slopes (being the inverse of the slopes of the lines shown). d) Complex-plane plots of the EIS data collected at 1.48 V vs. RHE; symbols show experimental data and dotted lines show simulated curves based on the parameters specified in Table S1. Data in panels (b)–(d) are shown as mean (lines in panel (b); symbols in panels (c) and (d)) and standard deviation (shading in panel (b); errors bars in panels (c) and (d)) derived from tests of $n = 3$ independent samples of each type. All potentials were post-corrected for ohmic losses; currents are normalized to the geometric surface area of the electrodes (1 cm^2).

comprising a very thin catalyst layer on a highly-conductive interconnected IO framework (Figure 2c).

Another parameter underpinning the advantageous performance of the electrodes based on the IO Cu framework is the enhanced catalytically active surface area. Indeed, NiFe LDH / Cu IO exhibit the highest among examined materials density of the redox active nickel-iron sites per geometric surface area (Figure 3a), as calculated by applying Faraday's law (assuming one-electron transfer) to the NiFe LDH catalyst reduction charge measured by voltammetry (inset in Figure 2a).[34] This observation is corroborated by the voltammetric measurements of the specific (pseudo)capacitance (Figures S10 and S11) and CPE parameters (Table S1).

Thus, the inverse opal substrate increases the density of the catalytically active sites by a factor of ca. 3 and 5 as compared to NiFe LDH IO and NiFe LDH / Cu TF, respectively. Furthermore, the specific OER activity normalized to both mass of the catalyst (i [A g^{-1}]) and number of the electrochemically active sites on its surface estimated from the voltammetric data[34] as explained above (presented as turn-over frequency, TOF [s^{-1}]) is also significantly higher for NiFe LDH / Cu IO (Figure 3b,c). Since the chemical nature of the catalytic component is identical in all examined materials, we attribute the observed enhancement of the specific OER activity of the NiFe LDH to the close proximity of the majority of the catalytic sites to the highly conductive IO support, which facilitates charge transfer and supports fast kinetics of water electrooxidation.

The NiFe LDH / Cu IO // FTO electrodes also outperform other reported inverse-opal OER catalysts based on flat substrates (Table S2). When compared to electrocatalysts supported on thick foam electrodes, which provide much higher active surface area than the flat FTO used herein, the NiFe LDH / Cu IO composite again demonstrates competitive performance, in particular at high current densities. For example, the NiFe LDH / Cu NWs // Cu foam[20] system with a specific (pseudo)capacitance of $C \approx 60$ mF cm^{-2} was reported to sustain the OER rate of 100 mA cm^{-2} at an overpotential just ~0.02 V lower than that measured herein for NiFe LDH / Cu IO having 50-fold lower $C \approx 1.2$ mF cm^{-2} (Table S2). A key feature that supports such advantageous performance of NiFe LDH / Cu IO at high current densities is the close-to-ideal Butler-Volmer current vs. potential behavior with one of the lowest Tafel slopes reported (Table S2).

The performance advantages provided by Cu IO are best emphasized through comparisons of the OER activity per unit mass of the catalyst and support (i [A g^{-1}]). For NiFe LDH / Cu IO // FTO, the catalyst + support loading was only 0.14 ± 0.04 mg cm^{-2}, more than an order of magnitude lower than for high-performance OER electrodes reported before (Table S2). This enables i values in excess of 100 A g^{-1} at

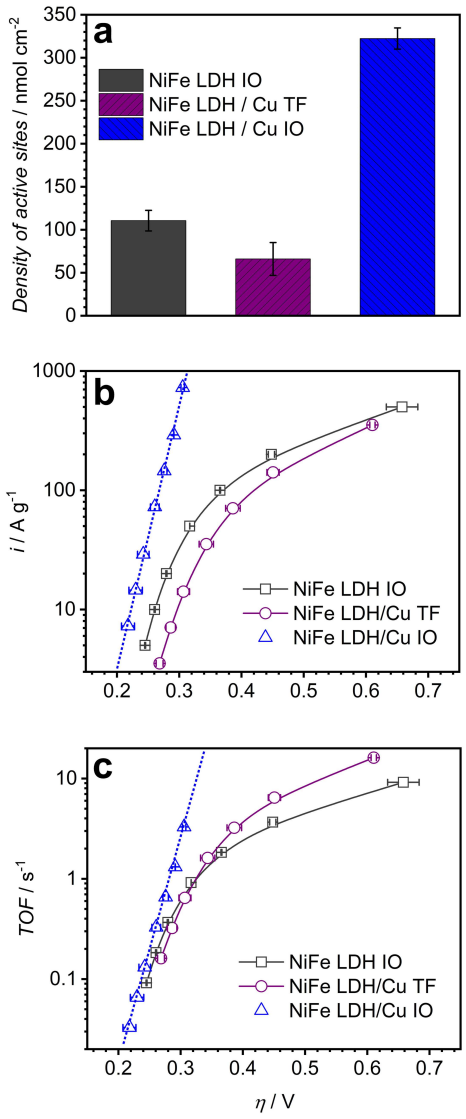

Figure 3. a) Surface density of redox-active NiFe sites (per geometric electrode surface area; 1 cm^2), b) specific OER catalytic activity per NiFe LDH + Cu unit mass, and c) turnover frequency of the OER for the NiFe LDH IO (grey), NiFe LDH / Cu TF (purple) and NiFe LDH / Cu IO (blue) catalysts. TOF values were calculated using the data in Figures 3c and 4a. In panels (c) and (d), dotted lines are linear fits to the data while grey and purple lines are guides to the eye. Data with error bars are mean ± one standard deviation derived from testing $n = 3$ independent samples of the same type; note that error bars are sometimes smaller than the symbols.

overpotential as low as *ca.* 0.27 V (Figure 3b), and much higher mass-normalized activity than other IO-based and foam-supported systems. For example, a high-performance NiFe LDH / NiFe NW catalyst supported on nickel foam was reported to achieve the OER rate of 100 mA cm^{-2} or ~40 A g^{-1} at $\eta \approx 0.27$ V,[17] while NiFe LDH / Cu IO enables the specific OER rate of 109 ± 6 A g^{-1} at the same overpotential (Figure 3b).

The durability of the NiFe LDH / Cu IO composites during water electrooxidation was assessed by chronopotentiometric tests at 10 and 100 mA cm^{-2} over 24 h (Figure 4a). At lower current density, the initial overpotential of ca. 0.26 V was stable throughout the experiment, while the higher reaction rate induced a slow increase in η from ~0.31 to ~0.35 V over the initial 16 h followed by stable operation. When comparing the OER polarization plots measured before and after 100 mA cm^{-2} tests, the deterioration in the activity was less significant (Figure 4b), which might be explained by the local decrease of pH during long-term OER occurring at a very high rate per the amount of NiFe catalyst used herein (Figure 3b).

Comparison of the Ni 2p and Fe 2p XP spectra before and after OER tests confirmed the XRD observations (Figure S5a) on the disappearance of the minor metallic admixtures and revealed no changes to the electronic states of the major hydroxide catalytic components (Figure S5c,d). However, quantitative XPS analysis indicated an increase in the Ni : Fe ratio (Figure S7d), which was found to be unfavorable for the OER activity of the system investigated herein (Figure S9). Nevertheless, it was clear that operation at 100 mA cm^{-2} did induce some changes to the electrode, which resulted in slightly suppressed, though still high, performance (Figure 4b). The only detectable change in XRD patterns was the disappearance of the initially weak diffraction peak attributed to metallic Ni/Fe, which was expected under strongly oxidative conditions, but no phase change of the Cu IO framework occurred (Figure S5a). Slight oxidation of the copper surface evidenced by the increased intensity of the shake-up satellite signal and higher-binding-energy shoulders in Cu 2p XP spectra is again attributed to small areas that are not fully covered with the NiFe LDH catalyst (Figure S5b). Besides, Cu^0 was still the dominating component, attesting to the very low thickness of the Cu^{2+} species formed during the continuous operation at positive potentials. These results are similar to those reported by Yu et al. for the NiFe LDH / Cu nanowire material even though the catalyst shell thickness was as high as 250 nm in that work[20] (cf. 85 ± 14 nm herein; Figure 1c).

These results were confirmed by inductively coupled plasma optical emission spectrometric analysis of the electrolyte solution before and after 100 mA cm^{-2} tests, which indicated a loss of 16.9 ± 0.4 at% Fe, while the decrease in the Ni content was 10.2 ± 0.1 at% (Figure 4d). There was also 6.1 ± 0.1 at% Cu loss during the operation, which is approximately 4.5-fold less than the combined corrosion of the NiFe LDH catalyst component, pointing to the latter as the major contributor to the loss of activity. Minor corrosion of the Cu IO is attributed to the areas not completely covered with NiFe LDH detected by XPS. SEM also confirmed the lack of detectable changes to the copper framework and thinning of the NiFe LDH layer accompanied by an increase in the average void size after operation at 100 mA cm^{-2} (Figure 4e and Figure S2e). Similar change was observed for NiFe LDH IO, indicating that it is an intrinsic property of the catalyst (Figure S15a,b). TEM and STEM-EDS analysis further confirmed the durability of Cu IO during tests at higher current density and partial distortion of the NiFe LDH nanosheets (Figure S16). Finally, the (pseudo)capacitance of layered double hydroxides (Figure S11) as well as the number of NiFe redox active sites (Figure 4c) decreased after the extended OER test by ca. 30 and 50%, respectively. Thus, all methods collectively suggest that partial loss of the activity of NiFe LDH / Cu IO is associated with changes in the nickel-iron

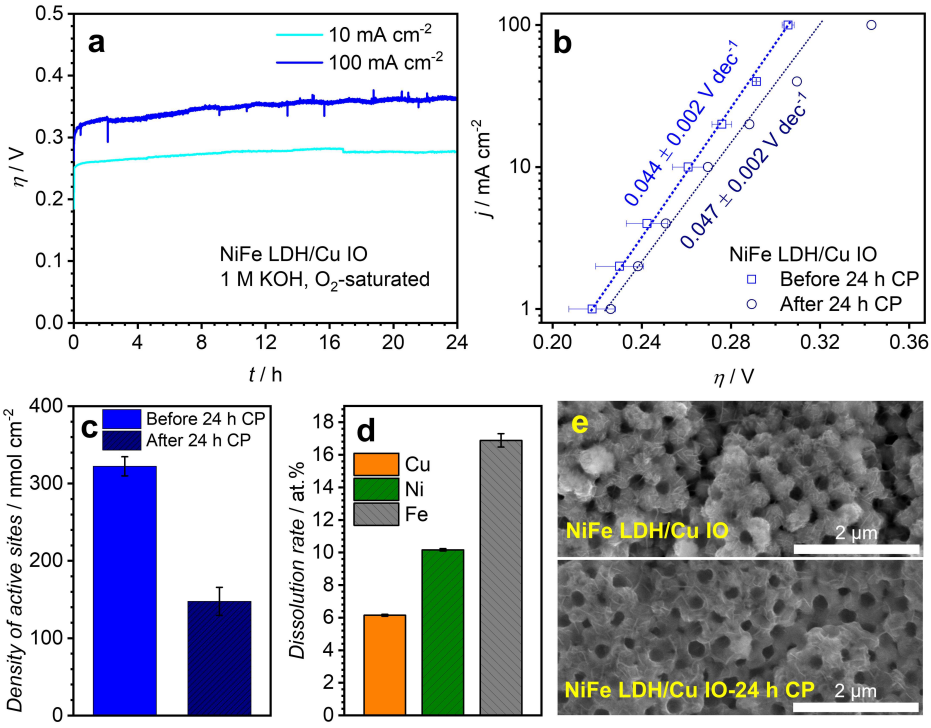

Figure 4. Stability of the FTO-supported NiFe LDH / Cu IO composite during the OER in O_2-saturated and continuously stirred 1 M KOH. a) iR_u-corrected transients of the OER overpotential recorded at 10 (cyan) and 100 mA cm^{-2} (blue). b) iR_u-corrected quasi-steady-state OER polarization data (symbols) recorded before (blue) and after (navy) 24 h tests at 100 mA cm^{-2} (corresponding chronopotentiograms are shown in Figure S14); lines show linear fits to the data. c) Number of active sites before (blue) and after (navy) the 24 h OER tests at 100 mA cm^{-2}. d) Loss of Cu (orange), Ni (green) and Fe (grey) after the 24 h OER tests at 100 mA cm^{-2} (shown as at % with respect to the initial amount of metals deposited on the electrode). e) Comparison of the SEM images of NiFe LDH / Cu IO before (top) and after (bottom) the 24 h OER test at 100 mA cm^{-2}.

hydroxide catalytic component but not the Cu IO support. It is important to note that the observed loss in the activity is not continuous, but the performance rather fluctuates during operation, probably due to the temporary changes in the local pH environment provided by the liquid electrolyte solution, as best seen in the data obtained during extended 100 h test (Figure S17). Importantly, the structure of the NiFe LDH / Cu IO catalyst was still maintained after 100 h of operation, as confirmed by STEM-EDS (Figure S18).

It is additionally important to note that the current density of 100 mA cm^{-2} used for the durability tests herein corresponds to the value of 727 ± 4 A g^{-1} per unit mass of the overall NiFe LDH / Cu IO material, or as high as 1070 ± 7 A g_{NiFe}^{-1} when normalized to the unit mass of the NiFe LDH catalytic component. The latter value is unprecedentedly high and likely pushes the limit of the catalytic capabilities of this particular material, as reflected by partial loss of the activity discussed above (Figure 4). These considerations suggest that integration of the inverse-opal-supported catalysts into practical AEM water electrolyzer devices operating at up to 1 A cm^{-2} current density will require corresponding increase in the thickness of the material, that is, by a factor of ca. 10. Considering that the thickness of NiFe LDH / Cu IO highlighted herein is only 2.2 ± 0.4 μm (Figure 1d), this adjustment is clearly achievable and is not expected to introduce any significant mass- or charge-transport limitations.

Conclusion

In summary, the present work introduces a metallic inverse opal framework as a highly effective support for oxygen evolution electrocatalysts. Having a thickness of only ca. 2 μm and mass loading of 0.14 ± 0.04 mg on a 1 cm^2 flat electrode, the Cu invers opal layer modified with the state-of-the-art nickel-iron layered double hydroxide catalyst exhibits an areal activity for water electrooxidation on par with that for 10^3-fold thicker foam-based electrodes of mm-scale thickness and loaded with several milligrams of the catalyst per cm^2. In other words, the use of highly favorable yet simple inverse-opal supports enables more than order of magnitude improvements in the specific OER catalytic activity and three-orders of magnitude thinning of the catalyst/electrode layer. This highlights another important feature of the IO catalysts as those highlighted herein, viz. their compatibility with membrane electrolyzers,[24] which require the use of catalyst layers of a micrometer-scale thickness for effective ion transport, which would not be possible with foam electrodes.

Thus, the inverse opal metallic frameworks present simple to fabricate supports that maximize the utilization of electrocatalysts deposited thereon and thereby enable outstanding performance. To achieve even better activity and stability, future work might use IO frameworks based on other metals like Ni and Fe as well as more advanced catalysts. We envisage

that such materials can be effective not only for the oxygen evolution reaction, but also for other electrocatalytic processes of applied significance.

Experimental Section

Materials and chemicals

Methyl methacrylate (Sigma), sodium dodecyl sulfate (>99%, Sigma), potassium peroxydisulfate (99.0% min, Alfa Aesar), acetone (Ajax-Finechem, Univar), ethanol (Absolute, Ajax-Finechem, Univar), propan-2-ol (AR Grade, Ajax-Finechem, Univar), dichloromethane (DCM, Sigma), ethyl acetate (AR Grade, Ajax-Finechem (Univar)), iron(II) sulfate heptahydrate (puriss. p.a., Sigma), nickel(II) sulfate hexahydrate (>98%, Sigma), copper(II) sulfate pentahydrate (EMSURE ACS, Sigma), sulfuric acid (98%, AJAX-Finechem, Univar), sulfuric acid (70%, AJAX-Finechem, Univar), potassium hydroxide (pellets for analysis EMSURE, Sigma), argon (99.99%, BOC), dinitrogen (99.99%, BOC) and dioxygen (99.99%, BOC) were all used as received.

Deionized water (Sartorius Arium Comfort I Ultrapure water system H2O–I-1-UV–T; resistivity 18.2 MΩ cm at 23 ± 2 °C) was used in all operations and for the preparation of all solutions.

Preparation of working electrode substrate

Fluorine doped tin oxide (FTO) (TEC8 Glass Plates, DyeSol) glass substrate was cut into 1 cm × 2 cm slides, washed with acetone, isopropanol and ethanol (15 min each step) by ultrasonication (Elmasonic, UC-7120L, 120 W), and then kept in 30 vol% ethanol in water. Before use, FTO slides were dried at 70 °C in oven for at least 30 min.

Synthesis of the poly(methylmethacrylate) beads

PMMA beads were synthesized by emulsion polymerization following a modified procedure adopted from the literature.[31] Water (98.0 mL) was degassed with nitrogen in a three necked flask for 1 h before the addition of the methyl methacrylate monomer (35.5 g, 0.35 mol) and sodium dodecyl sulfate surfactant (5.6 mg, 0.02 mmol). This mixture was stirred at 90 °C for 1 h under a nitrogen atmosphere to deactivate the inhibitors and obtain a homogenous emulsion. A solution of the potassium peroxydisulfate (56 mg, 0.2 mmol) in water (2.0 mL) was injected to initiate the polymerization reaction. The solution turned into a milky white dispersion within ~5 min indicating the formation of polymer particles. After 2 h at 90 °C, the flask was exposed to air, cooled on an ice bath, and left to stir overnight. The resulting colloidal dispersion was filtered through glass wool and washed with water three times by centrifugation (relative centrifugal force 9000, 30 min). Finally, the PMMA beads were obtained by drying the resulting solid compound in vacuum at ambient temperature.

Synthesis of the inverse opal frameworks and catalysts

General strategy to produce nickel-iron layered double hydroxide catalysts supported on the inverse-opal copper frameworks is summarized in Figure S1. CuIO frameworks were formed on FTO substrates modified with a PMMA opal template. To produce such templates, the PMMA microspheres were dispersed in water (120 mg/100 mL) by sonication for 3 h (Elmasonic, UC-7120L, 120 W), and FTO substrates (half of the surface was blocked with polyimide Kapton tape, that is, only an area of 1 cm × 1 cm was exposed to the solution) were placed horizontally at the bottom of the beaker containing the suspension. The template was formed through the self-assembly of dispersed PMMA opals on the substrate at 70 °C over 12 h. After unloading from the beaker, the PMMA//FTO substrates were gently cleaned with Kimwipe disposable wipers (KIMTECH) to remove the excess of PMMA, and dried in vacuum oven at ambient temperature for 1 h.

The PMMA//FTO substrates were used as electrodes for the electrodeposition of Cu from quiescent 0.2 M $CuSO_4$ + 0.01 M H_2SO_4 aqueous solution pre-saturated with Ar (for 1 h under continuous stirring) at −1 V vs. Ag|AgCl|$KCl_{sat.}$ reference electrode (CH Instruments, Inc.) for 60 s using high-surface area coiled Cu wire as an auxiliary electrode in a single-compartment Pyrex glass cell. After deposition, the electrodes were copiously rinsed with ethanol, and the PMMA opal template was removed by soaking in pure dichloromethane overnight (ca. 15–20 h). After washing with ethyl acetate and acetone, the resulting CuIO//FTO substrates were used for deposition of the OER catalyst. Weighing of the FTO before and after modification with CuIO (Mettler Toledo, NewClassic MF, MS105DU) indicated that the mass of the deposited copper framework was 0.045 ± 0.003 mg cm^{-2}. The same value was obtained by dissolving the CuIO framework from several control samples in 10 mL of HNO_3 (35%) and subsequent analysis by inductively coupled plasma optical emissions spectroscopy (ICP-OES) (see below).

NiFeLDH were produced on the CuIO framework surface by reductive electrodeposition from quiescent 0.05 M $FeSO_4$ + 0.05 M $NiSO_4$ aqueous solution (pH 5.5) pre-saturated with Ar (for 1 h under continuous stirring) at −1 V vs. Ag|AgCl|$KCl_{sat.}$ reference electrode for 90 s using Pt wire as an auxiliary electrode in a single-compartment Pyrex glass cell. The obtained NiFeLDH/CuIO electrodes were washed with deionized water, dried in air, and stored in a Petri dish before use.

Additionally, two types of control electrodes were synthesized: one by electrodepositing a thin film (TF) of Cu onto a PMMA-free FTO followed by modification with NiFeLDH (NiFeLDH/CuTF), and another by direct electrodeposition of NiFeLDH onto the PMMA-modified FTO to produce NiFeLDHIO materials with no copper substrate. All procedures used for these samples were identical to those described above, except for the electrodeposition time of NiFeLDHIO, which was extended to 2 min to produce sufficiently thick framework.

After the final electrodeposition step, washed and dried electrodes were weighed using microbalance (Mettler Toledo, NewClassic MF, MS105DU) to determine the amount of the material (Cu and/or NiFeLDH) deposited. The recorded mass loadings per FTO geometric surface area were 0.20 ± 0.02, 0.28 ± 0.01 and 0.14 ± 0.04 mg cm^{-2} for NiFeLDHIO, NiFeLDH/CuTF and NiFeLDH/CuIO, respectively. The catalyst + support loading for several NiFeLDH/CuIO control samples was additionally measured by ICP-OES, and the results were in a perfect agreement with the gravimetric analysis for both types of samples.

Physical characterization

X-ray diffraction analysis was undertaken using a Bruker D8 Advance Eco Diffractometer equipped with a 1000 W Co K_α X-ray source (λ = 0.179 nm) and Fe K_β filter. The samples (cut to the size of 0.5 cm × 1 cm) were mounted on a sample holder using an adhesive. The XRD measurement was performed using 1 mm Fe slit, 0.02° step size, 15 rpm sample rotation speed and X-ray incident angle of 5°.

Scanning electron microscopic coupled to *energy dispersive X-ray spectroscopic* analysis was performed using a field emission scanning electron microscope (FEI Quanta 3D FIBSEM) equipped with a EDAX Pegasus and TEAM X-ray analysis system as well as 10 mm^2 SDD with ultra-thin window. The samples (0.5 cm × 1 cm in size) were mounted onto a SEM sample holder using double-sided sticky carbon tape. No additional coatings were applied to the SEM samples, except for the PMMA-modified FTO which was modified with sputtered carbon. The cross-sectional SEM images were obtained using a SEM X-Section Holder (set screw vise 12.7 mm, 16350 Ted Pella).

Transmission electron micrographs and *scanning transmission electron micrographs* were collected using FEI Tecnai G2 T20 (200 kV; LaB_6 emitter) and FEI Tecnai F20 FEGTEM (200 kV; Super-Twin lens; coupled with Gatan EDX DigitalMicrograph) instruments, respectively. The samples were exfoliated from the FTO substrate, dispersed in ethanol by ultra-sonication (Elmasonic, UC-7120L, 120 W) for 15 min, drop-cast onto a carbon-coated copper grid (Lacey Carbon film 300 mesh copper; LC300Cu25 Emgrid) and dried overnight before TEM imaging.

X-ray photoelectron spectroscopic analysis was conducted using a Thermo Scientific Nexsa Surface Analysis System for samples cut to 0.5 cm × 1 cm size, that had no electrical contact with the instrument ground. XPS measurements were undertaken using a monochromated Al K_α source (1486.6 eV) at a power of 72 W (12 kV × 6 mA) and X-ray spot size of 400 μm × 800 μm, with the main chamber pressure not worse than 10^{-8} mbar. The survey scans were recorded at a pass energy of 200 eV with a step size of 1 eV, while the high-resolution spectra were acquired at 50 eV pass energy and 0.1 eV step size. Data processing was conducted using Avantage software (version 5.9902). Binding energies were referenced to the main aliphatic C 1 s peak at 284.8 eV. The surface elemental composition was estimated based on the integral peak intensities using the sensitive factors provided by the manufacturer.

Electrochemical characterization

Electrochemical experiments were undertaken using a VSP Biologic electrochemical workstation in a three-electrode configuration at ambient temperature (23 ± 2 °C). A custom-made two-compartment hermetic Teflon cell equipped with a gas in/outlets and sealed electrode ports was employed for the OER experiments and electrode characterization. Prior to use, the cell and all labware used for the experiments were cleaned by soaking in ethanol for at least 1 h and subsequent washing with copious amounts of water. Aqueous 1 M KOH saturated with O_2 by purging the gas for 15 min before the measurements and then continuously purged through the solution during the experiment was used as an electrolyte solution. The electrolyte solution was continuously stirred during the electrochemical measurements at 1000 rpm (2 mm × 10 mm Teflon-coated stirring bar). The volume of the electrolyte solution in the working electrode compartment was 20 mL.

Platinum plate (1 cm × 2 cm; Latech) and Hg | HgO | 1 M KOH (Latech) were used as auxiliary and reference electrodes, respectively. Reference electrode was positioned at a fixed distance of ca. 10 mm from the working electrode surface. The Hg | HgO | 1 M KOH reference system was calibrated by measuring its potential against a custom-made reversible hydrogen electrode (RHE; platinized platinum in H_2-saturated 1 M KOH under 1 atm H_2 pressure[38]). Thereby, all potentials in this manuscript are reported on a reversible hydrogen electrode scale ($E_{Hg/HgO} = 0.927$ V vs. RHE).

Electrochemical impedance spectra (EIS; 0.010 V amplitude, 100 kHz–0.1 Hz frequency range) were recorded at potentials where no significant faradaic processes occur to determine uncompensated resistance (R_u) before and after each set of electrochemical measurements. Unless specifically mentioned, potentials are reported after manual post-correction for the iR_u product.

Electrodes of each type were synthesized and tested as at least 3 independent samples, and the corresponding electrochemical data are reported as mean ± standard deviation.

Inductively coupled plasma optical emission spectroscopy

ICP-OES analysis was performed using a PerkinElmer Avio 200 instrument at 327.393 (Cu), 341.476 (Ni) and 238.204 nm (Fe). Raw analyte counts were standardized using a calibration curve constructed through dilutions of commercial stock solutions (Sigma-Aldrich) to concentrations in the 0.001–100 μg mL^{-1} range in 2 wt% HNO_3. After recording the initial 3 voltammetric cycles, the electrolyte solution in the cell was replaced with a fresh portion of 1 M KOH to avoid a contribution of loosely bound species to the final result, and a 24 h test at 100 mA cm^{-2} was run. Upon completion, the whole volume of the electrolyte solution was acidified with 70% HNO_3 to pH ≈ 1 and kept at 70 °C under continuous stirring for 1 h to ensure complete dissolution of metal hydroxides before the analysis. Finally, the samples were diluted two-fold with 2 wt% HNO_3, which was also used as a carrier solution for ICP-OES. Background was measured by analyzing pure 2 wt% HNO_3 and these counts were subtracted from all data.

Supporting Information

Supporting Information is available from the Wiley Online Library or from the author.

Acknowledgements

The authors acknowledge the use of facilities within the Monash X-ray Platform and Monash Centre for Electron Microscopy (Monash University). This work was funded by the Commonwealth Government of Australia through the Commonwealth Research Centres Projects (CRC-P) Grants program (Project – "Developing Next Generation Hydrogen Energy System", through Energys Australia Pty Ltd), Energys Australia Ptry Ltd, and Australian Research Council through a Future Fellowship to ANS (FT200100317). Open Access publishing facilitated by Monash University, as part of the Wiley - Monash University agreement via the Council of Australian University Librarians.

Conflict of Interest

T.D.N. and J.F.V. are employees of Energys. J.F.V. is a shareholder and option holder in Energys.

Data Availability Statement

Data that support the findings of this study are available from the corresponding author upon a reasonable request.

Keywords: copper · electrical conductivity · layered double hydroxides · mass transport · oxygen evolution reaction

[1] D. R. MacFarlane, J. Choi, B. H. R. Suryanto, R. Jalili, M. Chatti, L. M. Azofra, A. N. Simonov, *Adv. Mater.* **2020**, *32*, 1904804.
[2] a) J. Kibsgaard, I. Chorkendorff, *Nat. Energy* **2019**, *4*, 430; b) W. Seh Zhi, J. Kibsgaard, F. Dickens Colin, I. Chorkendorff, K. Nørskov Jens, F. Jaramillo Thomas, *Science* **2017**, *355*, eaad4998.
[3] a) Thyssenkrupp, "Hydrogen: an energy carrier for the future", can be found under https://hydrogen.thyssenkrupp.com/en/, **2021**; b) S. AG, "The power of Hydrogen", can be found under https://www.siemens-energy.com/global/en/offerings/renewable-energy/hydrogen-solutions.html, **2021**.
[4] a) J. Wang, Y. Gao, H. Kong, J. Kim, S. Choi, F. Ciucci, Y. Hao, S. Yang, Z. Shao, J. Lim, *Chem. Soc. Rev.* **2020**, *49*, 9154; b) L. Li, P. Wang, Q. Shao, X. Huang, *Adv. Mater.* **2021**, *33*, 2004243; c) C. Walter, P. W. Menezes, M. Driess, *Chem. Sci.* **2021**, *12*, 8603; d) H. Yang, M. Driess, P. W. Menezes, *Adv. Energy Mater.* **2021**, *11*, 2102074.
[5] a) N. Guillet, P. Millet, in *Hydrogen Production* (Eds.: A. Godula-Jopek), **2015**, 117; b) M. David, C. Ocampo-Martínez, R. Sánchez-Peña, *J. Energy Storage* **2019**, *23*, 392.
[6] I. Vincent, D. Bessarabov, *Renewable Sustainable Energy Rev.* **2018**, *81*, 1690.
[7] Y. Chen, K. Rui, J. Zhu, S. X. Dou, W. Sun, *Chem. Eur. J.* **2019**, *25*, 703.
[8] a) M. Gong, Y. Li, H. Wang, Y. Liang, J. Z. Wu, J. Zhou, J. Wang, T. Regier, F. Wei, H. Dai, *J. Am. Chem. Soc.* **2013**, *135*, 8452; b) M. Chatti, A. M. Glushenkov, T. Gengenbach, G. P. Knowles, T. C. Mendes, A. V. Ellis, L. Spiccia, R. K. Hocking, A. N. Simonov, *Sustain. Energy Fuels* **2018**, *2*, 1561; c) B. W. Xue, C. H. Zhang, Y. Z. Wang, W. W. Xie, N.-W. Li, L. Yu, *Nanoscale Adv.* **2020**, *2*, 5555; d) M. Wilhelm, A. Bastos, C. Neves, R. Martins, J. Tedim, *Mater. Des.* **2021**, *212*, 110188; e) F. Song, X. Hu, *Nat. Commun.* **2014**, *5*, 4477.
[9] X. Lu, H. Xue, H. Gong, M. Bai, D. Tang, R. Ma, T. Sasaki, *Nano-Micro Lett.* **2020**, *12*, 86.
[10] a) J. Zhao, J.-J. Zhang, Z.-Y. Li, X.-H. Bu, *Small* **2020**, *16*, 2003916; b) D. Friebel, M. W. Louie, M. Bajdich, K. E. Sanwald, Y. Cai, A. M. Wise, M.-J. Cheng, D. Sokaras, T.-C. Weng, R. Alonso-Mori, R. C. Davis, J. R. Bargar, J. K. Nørskov, A. Nilsson, A. T. Bell, *J. Am. Chem. Soc.* **2015**, *137*, 1305; c) Z. Li, M. Shao, H. An, Z. Wang, S. Xu, M. Wei, D. G. Evans, X. Duan, *Chem. Sci.* **2015**, *6*, 6624.
[11] a) X. Long, Z. Wang, S. Xiao, Y. An, S. Yang, *Mater. Today* **2016**, *19*, 213; b) L. Lv, Z. Yang, K. Chen, C. Wang, Y. Xiong, *Adv. Energy Mater.* **2019**, *9*, 1803358; c) Y. Wang, D. Yan, S. El Hankari, Y. Zou, S. Wang, *Adv. Sci.* **2018**, *5*, 1800064.
[12] a) O. V. Cherstiouk, V. L. Kuznetsov, A. N. Simonov, I. N. Mazov, K. V. Elumeeva, N. S. Moseva, *Phys. Status Solidi B* **2010**, *247*, 2738; b) O. V. Cherstiouk, A. N. Simonov, N. S. Moseva, S. V. Cherepanova, P. A. Simonov, V. I. Zaikovskii, E. R. Savinova, *Electrochim. Acta* **2010**, *55*, 8453; c) S. Maass, F. Finsterwalder, G. Frank, R. Hartmann, C. Merten, *J. Power Sources* **2008**, *176*, 444; d) S. Möller, S. Barwe, J. Masa, D. Wintrich, S. Seisel, H. Baltruschat, W. Schuhmann, *Angew. Chem. Int. Ed.* **2020**, *59*, 1585; e) S. Möller, S. Barwe, S. Dieckhöfer, J. Masa, C. Andronescu, W. Schuhmann, *ChemElectroChem* **2020**, *7*, 2680.
[13] a) L. Wang, F. Song, G. Ozouf, D. Geiger, T. Morawietz, M. Handl, P. Gazdzicki, C. Beauger, U. Kaiser, R. Hiesgen, A. S. Gago, K. A. Friedrich, *J. Mater. Chem. A* **2017**, *5*, 3172; b) B. Han, M. Risch, S. Belden, S. Lee, D. Bayer, E. Mutoro, Y. Shao-Horn, *J. Electrochem. Soc.* **2018**, *165*, F813; c) J. Cheng, J. Yang, S. Kitano, G. Juhasz, M. Higashi, M. Sadakiyo, K. Kato, S. Yoshioka, T. Sugiyama, M. Yamauchi, N. Nakashima, *ACS Catal.* **2019**, *9*, 6974; d) L. Moriau, M. Bele, Ž. Marinko, F. Ruiz-Zepeda, G. Koderman Podboršek, M. Šala, A. K. Šurca, J. Kovač, I. Arčon, P. Jovanovič, N. Hodnik, L. Suhadolnik, *ACS Catal.* **2021**, *11*, 670; e) A. Peugeot, C. E. Creissen, D. Karapinar, H. N. Tran, M. Schreiber, M. Fontecave, *Joule* **2021**, *5*, 1281; f) H.-S. Oh, H. N. Nong, T. Reier, A. Bergmann, M. Gliech, J. Ferreira de Araújo, E. Willinger, R. Schlögl, D. Teschner, P. Strasser, *J. Am. Chem. Soc.* **2016**, *138*, 12552; g) G. C. da Silva, S. I. Venturini, S. Zhang, M. Löffler, C. Scheu, K. J. J. Mayrhofer, E. A. Ticianelli, S. Cherevko, *ChemElectroChem* **2020**, *7*, 2330.
[14] Z. Lu, W. Xu, W. Zhu, Q. Yang, X. Lei, J. Liu, Y. Li, X. Sun, X. Duan, *Chem. Commun.* **2014**, *50*, 6479.
[15] Z. Wang, S. Zeng, W. Liu, X. Wang, Q. Li, Z. Zhao, F. Geng, *ACS Appl. Mater. Interfaces* **2017**, *9*, 1488.
[16] J. Liu, J. Wang, B. Zhang, Y. Ruan, L. Lv, X. Ji, K. Xu, L. Miao, J. Jiang, *ACS Appl. Mater. Interfaces* **2017**, *9*, 15364.
[17] C. Liang, P. Zou, A. Nairan, Y. Zhang, J. Liu, K. Liu, S. Hu, F. Kang, H. J. Fan, C. Yang, *Energy Environ. Sci.* **2020**, *13*, 86.
[18] B. Wang, S. Jiao, Z. Wang, M. Lu, D. Chen, Y. Kang, G. Pang, S. Feng, *J. Mater. Chem. A* **2020**, *8*, 17202.
[19] a) J. Chen, Q. Long, K. Xiao, T. Ouyang, N. Li, S. Ye, Z.-Q. Liu, *Sci. Bull.* **2021**, *66*, 1063; b) X.-P. Li, L.-R. Zheng, S.-J. Liu, T. Ouyang, S. Ye, Z.-Q. Liu, *Chin. Chem. Lett.* **2022**, *33*, 4761–4765..
[20] L. Yu, H. Zhou, J. Sun, F. Qin, F. Yu, J. Bao, Y. Yu, S. Chen, Z. Ren, *Energy Environ. Sci.* **2017**, *10*, 1820.
[21] H. Wang, T. Zhou, P. Li, Z. Cao, W. Xi, Y. Zhao, Y. Ding, *ACS Sustainable Chem. Eng.* **2018**, *6*, 380.
[22] P. Zhao, H. Nie, Z. Zhou, J. Wang, G. Cheng, *ChemistrySelect* **2018**, *3*, 8064.
[23] Y.-J. Huang, C.-H. Lai, P.-W. Wu, L.-Y. Chen, *J. Electrochem. Soc.* **2010**, *157*, P18.
[24] J. E. Park, S. Kim, O.-H. Kim, C.-Y. Ahn, M.-J. Kim, S. Y. Kang, T. I. Jeon, J.-G. Shim, D. W. Lee, J. H. Lee, Y.-H. Cho, Y.-E. Sung, *Nano Energy* **2019**, *58*, 158.
[25] S. A. Cho, Y. J. Jang, H.-D. Lim, J.-E. Lee, Y. H. Jang, T.-T. H. Nguyen, F. M. Mota, D. P. Fenning, K. Kang, Y. Shao-Horn, D. H. Kim, *Adv. Energy Mater.* **2017**, *7*, 1700391.
[26] C.-T. Hsieh, C.-L. Huang, Y.-A. Chen, S.-Y. Lu, *Appl. Catal. B* **2020**, *267*, 118376.
[27] Q. Zhou, J. Pu, X. Sun, C. Zhu, J. Li, J. Wang, S. Chang, H. Zhang, *J. Mater. Chem. A* **2017**, *5*, 14873.
[28] D. Böhm, M. Beetz, M. Schuster, K. Peters, A. G. Hufnagel, M. Döblinger, B. Böller, T. Bein, D. Fattakhova-Rohlfing, *Adv. Funct. Mater.* **2020**, *30*, 1906670.
[29] P.-S. Hung, W.-A. Chung, S.-C. Chou, K.-C. Tso, C.-K. Chang, G.-R. Wang, W.-Q. Guo, S.-C. Weng, P.-W. Wu, *Catal. Sci. Technol.* **2020**, *10*, 7566.
[30] Merck, "Micro particles based on polystyrene", can be found under https://www.sigmaaldrich.com/AU/en/product/sial/72986, **2022**.
[31] a) D. Zou, S. Ma, R. Guan, M. Park, L. Sun, J. J. Aklonis, R. Salovey, *J. Polym. Sci. Part A* **1992**, *30*, 137; b) K. Peters, P. Zeller, G. Stefanic, V. Skoromets, H. Němec, P. Kužel, D. Fattakhova-Rohlfing, *Chem. Mater.* **2015**, *27*, 1090.
[32] a) G. Cheng, A. R. Hight Walker, *Anal. Bioanal. Chem.* **2010**, *396*, 1057; b) Y. Liang, S. C. Oh, X. Wang, H. Glicksman, D. Liu, S. Ehrman, *RSC Adv.* **2017**, *7*, 23468.
[33] a) Y. Zhu, W. Chu, N. Wang, T. Lin, W. Yang, J. Wen, X. S. Zhao, *RSC Adv.* **2015**, *5*, 77958; b) M. Jamal, S. Chakrabarty, H. Shao, D. McNulty, M. A. Yousuf, H. Furukawa, A. Khosla, K. M. Razeeb, *Microsyst. Technol.* **2018**, *24*, 4217.
[34] L. Trotochaud, S. L. Young, J. K. Ranney, S. W. Boettcher, *J. Am. Chem. Soc.* **2014**, *136*, 6744.
[35] M. C. Biesinger, *Surf. Interface Anal.* **2017**, *49*, 1325.
[36] a) M. C. Biesinger, B. P. Payne, A. P. Grosvenor, L. W. M. Lau, A. R. Gerson, R. S. C. Smart, *Appl. Surf. Sci.* **2011**, *257*, 2717; b) M. C. Biesinger, L. W. M. Lau, A. R. Gerson, R. S. C. Smart, *Phys. Chem. Chem. Phys.* **2012**, *14*, 2434.
[37] S. Anantharaj, S. Kundu, S. Noda, *J. Electrochem. Soc.* **2022**, *169*, 014508.
[38] D. Simondson, M. Chatti, S. A. Bonke, M. F. Tesch, R. Golnak, J. Xiao, D. A. Hoogeveen, P. V. Cherepanov, J. L. Gardiner, A. Tricoli, D. R. MacFarlane, A. N. Simonov, *Angew. Chem. Int. Ed.* **2021**, *60*, 15821.

Manuscript received: May 3, 2022
Revised manuscript received: July 22, 2022
Accepted manuscript online: July 25, 2022
Version of record online: September 23, 2022